

# Molecule States in a Gate Tunable Graphene Double Quantum Dot

Lin-Jun Wang, Hai-Ou Li, Zhan Su, Tao Tu,\* Gang Cao, Cheng

Zhou, Xiao-Jie Hao, Guang-Can Guo, and Guo-Ping Guo†

*Key Laboratory of Quantum Information,*

*University of Science and Technology of China,*

*Chinese Academy of Sciences, Hefei 230026, People's Republic of China*

(Dated: October 29, 2018)

## Abstract

We have measured a graphene double quantum dot device with multiple electrostatic gates that are used to enhance control to investigate it. At low temperatures the transport measurements reveal honeycomb charge stability diagrams which can be tuned from weak to strong interdot tunnel coupling regimes. We precisely extract a large interdot tunnel coupling strength for this system allowing for the observation of tunnel-coupled molecular states extending over the whole double dot. This clean, highly controllable system serves as an essential building block for quantum devices in a nuclear-spin-free world.

---

\*Electronic address: tutao@ustc.edu.cn

†Electronic address: gpguo@ustc.edu.cn

Graphene exhibits novel electrical properties and offers substantial potential as building blocks of nanodevices owing to its unique two-dimensional structure [1–3]. Besides being a promising candidate for high performance electronic devices, graphene may also be used in the field of quantum computation, which involves exploration of the extra degrees of freedom provided by electron spin, in addition to those due to electron charge. During the past few years significant progress has been achieved in implementation of electron spin qubits in semiconductor quantum dots [4, 5]. To realize quantum computation, the effects of interactions between qubits and their environment must be minimized [6]. Because of the weak spin-orbit coupling and largely eliminated hyperfine interaction in graphene, it is highly desirable to coherently control the spin degree of freedom in graphene nanostructures for quantum computation [7, 8]. Recently, there was a striking advance on experimental production of graphene single or double quantum dots [9–12], which is an important first step towards such promise.

Here we report an experimental demonstration and electrical transport measurement in a tunable graphene double quantum dot device. Depending on the strength of the interdot coupling, the device can form atomiclike states on the individual dots (weak tunnel coupling) or molecularlike states of the two dots (strong tunnel coupling). We also extract the interdot tunnel coupling by identifying and characterizing the molecule states with wave functions extending over the whole graphene double dot. The result implies that this artificial graphene device may be useful for implementing two-electron spin manipulation.

The graphene flakes were produced by mechanical cleaving of graphite crystallites by scotch tape and then were transferred to a highly doped Si substrate with a 100 nm SiO<sub>2</sub> top layer. Thin flakes were found by optical microscopy and single layer graphene flakes were selected by the Raman spectroscopy measurement. Next, a layer of poly(methyl methacrylate) (PMMA) was exposed by standard electron beam lithography (EBL) to form a designed pattern. The unprotected areas were carved by oxygen reactive ion etching. We used the standard EBL and lift off technique to make the ohmic contact (Ti/Au) on the present graphene device. A scanning electron microscope image of our defined sample structure with double quantum dot is shown in Figure 1. The double quantum dot has two isolated central island of diameter 100 nm in series, connected by 20 × 20 nm narrow constriction to source and drain contacts (S and D electrodes) and 30 × 20 nm narrow constriction with each other. These constrictions are expected to act as tunnel barriers due to the quantum

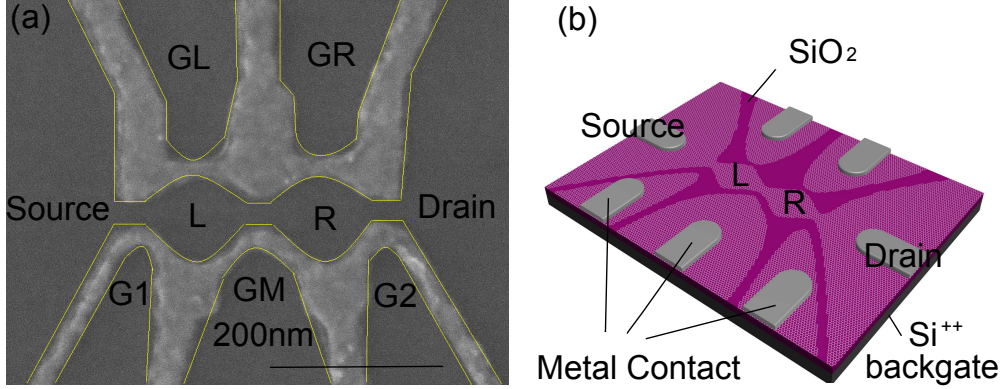


FIG. 1: (a) Scanning electron microscope image of the structure of the designed multiple gated sample studied in this work. The double quantum dot have two isolated central islands of diameter 100 nm in series, connected by  $20 \times 20$  nm tunneling barriers to source and drain contacts (S and D) and  $30 \times 20$  nm tunneling barrier with each other. These gates are labeled by G1, GL, GM, GR, G2, in which gate GM, G1 and G2, are used to control the coupling barriers between the dots as well as the leads. Gates GL and GR are used to control and adjust the energy level of each dot. (b) Schematic of a representative device.

size effect. In addition, the highly P-doped Si substrate is used as a back gate and five lateral side gates, labeled the left gate G1, right gate G2, center gate GM and GL(R), which are expected for local control. All of side gates are effective, in which gates GL, GR and G2 have very good effect on two dots and middle barrier, while gates G1 and GM have weak effect on those. The device was first immersed into a liquid helium storage dewar at 4.2 K to test the functionality of the gates. The experiment was carried out in a He3 cryostat equipped with filtered wiring and low-noise electronics at the base temperature of 300 mK. In the measurement, we employed the standard AC lock-in technique with an excitation voltage  $20 \mu\text{V}$  at 11.3 Hz.

Fig. 2(a) displays the differential conductance through the graphene double quantum dot circuit as a function of gate voltages  $V_{GL}$  and  $V_{GR}$ . Here the measurement was recorded at  $V_{sd} = 20 \mu\text{V}$ ,  $V_{G1} = 0 \mu\text{V}$ ,  $V_{GM} = 0 \mu\text{V}$ ,  $V_{G2} = 0 \mu\text{V}$  and  $V_{bg} = 2.5 \text{V}$ . The honeycomb pattern is clearly visible and uniforms over many times. Each cell of the honeycomb corresponds to a well-defined charge configuration  $(N_L, N_R)$  in the nearly independent dots, where  $N_L$  and  $N_R$  denote the number of electrons on the left and right dot, respectively. The conductance is large at the vertices, where the electrochemical potentials in both dots are aligned with

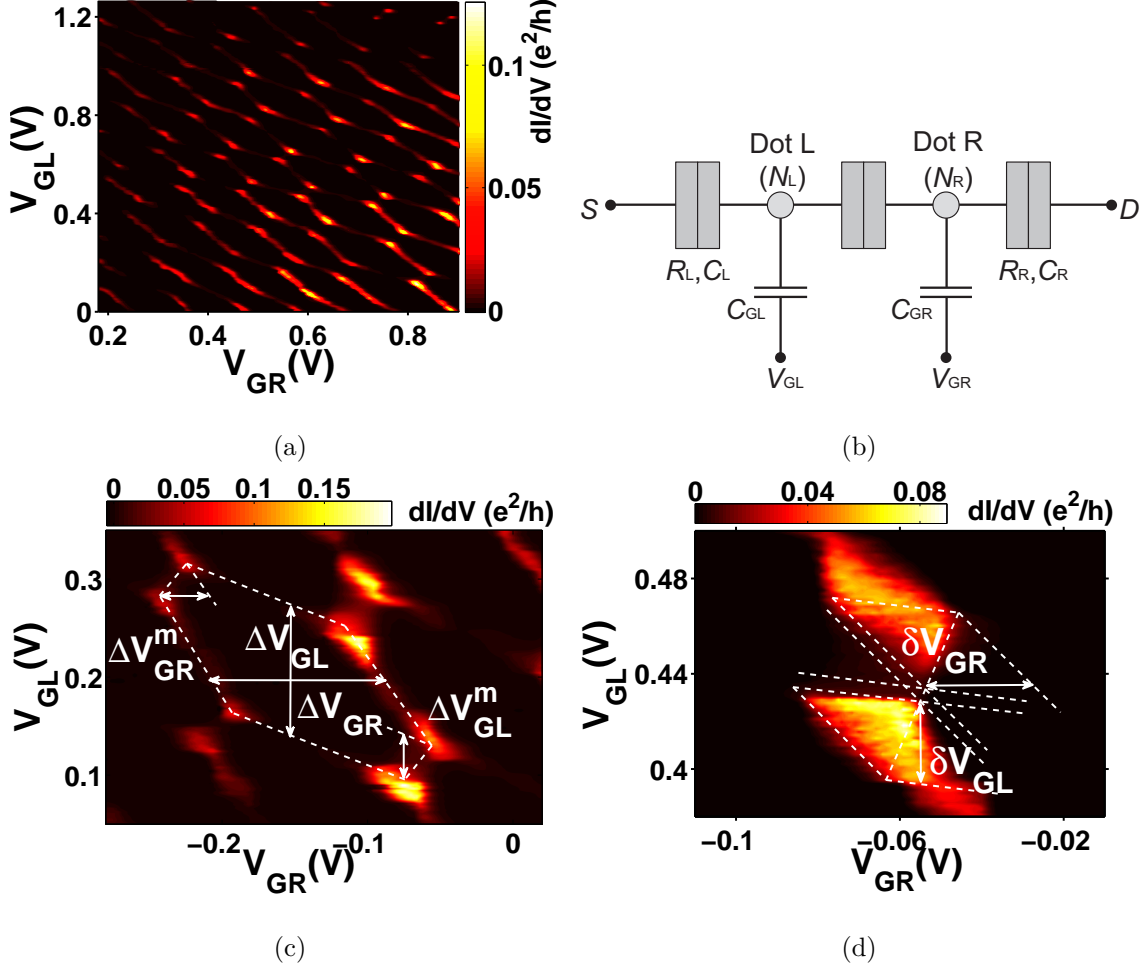


FIG. 2: (a) Colorscale plot of the differential conductance versus voltage applied on gate GL ( $V_{GL}$ ) and gate GR ( $V_{GR}$ ) at  $V_{sd} = 20 \mu\text{V}$ ,  $V_{G1} = 0 \mu\text{V}$ ,  $V_{GM} = 0 \mu\text{V}$  and  $V_{G2} = 0 \mu\text{V}$ . The honeycomb pattern we got stands for the typical charge stability diagram of coupled double quantum dots. (b) Pure capacitance model of a graphene double dot system. Zoom-in of a honeycomb structure (c) and a vertex pair (d) at  $V_{sd} = 900 \mu\text{V}$ .

each other and the Fermi energy in the leads and resonant sequential tunneling is available. These vertices are connected by faint lines of much smaller conductance along the edges of the honeycomb cells. At these lines, the energy level in one dot is aligned with the electrochemical potential in the corresponding lead and inelastic cotunneling processes occur. The observed honeycomb pattern resembles the charge stability diagram found for weakly coupled GaAs double quantum dot [13]. Such similarities indicate that graphene quantum dot devices will continue to share features with well-studied semiconductor quantum dot

systems.

More quantitative information such as double dot capacitances can be extracted using an electrostatic model [13]. First, the capacitance of the dot to the side gate can be determined from measuring the size of the honeycomb in Fig. 2(b) as  $C_{GL} = e/\Delta V_{GL} \approx 1.27$  aF and  $C_{GR} = e/\Delta V_{GR} \approx 1.49$  aF. Next, the capacitance ratios can be determined from measuring the size of the vertices in Fig. 2(b) at finite bias  $V_{sd} = 900 \mu\text{V}$  as  $\alpha_L = |V_{sd}|/\delta V_{GL} = 0.029$  and  $\alpha_R = |V_{sd}|/\delta V_{GR} \approx 0.035$ . Using the relation  $C_{GL}/C_L = \alpha_L$  and  $C_{GR}/C_R = \alpha_R$ , we can obtain the typical values of dot capacitances as  $C_L \approx 44.8$  aF and  $C_R \approx 44.1$  aF, respectively. The amount of interdot coupling can be achieved by measuring the vertices splitting in Fig. 2(c). Assuming the capacitively coupling is dominant in the weakly coupled dots regime [13, 14], the mutual capacitance between dots is calculated as  $C_m = \Delta V_{GL}^m C_{GL} C_R / e = \Delta V_{GR}^m C_{GR} C_L / e \approx 9.2$  aF.

It has been expected that opening the interdot constriction by gate voltage will cause the tunnel coupling to increase exponentially faster than the capacitive coupling [15]. Fig. 3(a)-(c) represent a selection of such measurements by holding the same  $V_{GR}$  and  $V_{bg}$  and scanning different ranges of  $V_{GL}$  between  $-0.5$  V to  $0.35$  V. An evolution of conductance pattern indicates that the stability diagram changes from weak to strong tunneling regimes [13, 14]. The conductance near the vertices depends on the relative contributions of the capacitive coupling and tunnel coupling. For the former, the vertices become a sharpened point, while for the latter, the vertices become blurred along the edges of the honeycomb cell [16]. In Fig. 3(b), the vertices are not obvious as those in Fig. 3(a), which indicates a stronger tunnel coupling. The results suggest that two graphene dots are interacting with each other through the large quantum mechanical tunnel coupling, which is analogous to covalent bonding. We will analyze it in details below. An increase in interdot coupling also leads to much larger separation of vertices in Fig. 3(b) [14], and finally, to a smearing of honeycomb features in Fig. 3(c). In this case, the double dots behave like a single dot. We note that a similar evolution is observed for four different values of  $V_{bg}$  from  $2.5$  V to  $2.0$  V at the same  $V_{GL}$  and  $V_{GR}$  regimes. Thus the interdot tunnel coupling could also be changed by  $V_{GL}$  or  $V_{bg}$ . This can be explained by the fact that the side gates and back gate may influence the central barrier through the existing capacitances between the gates and the central barrier.

Having understood the qualitative behavior of the graphene device in the strong coupling

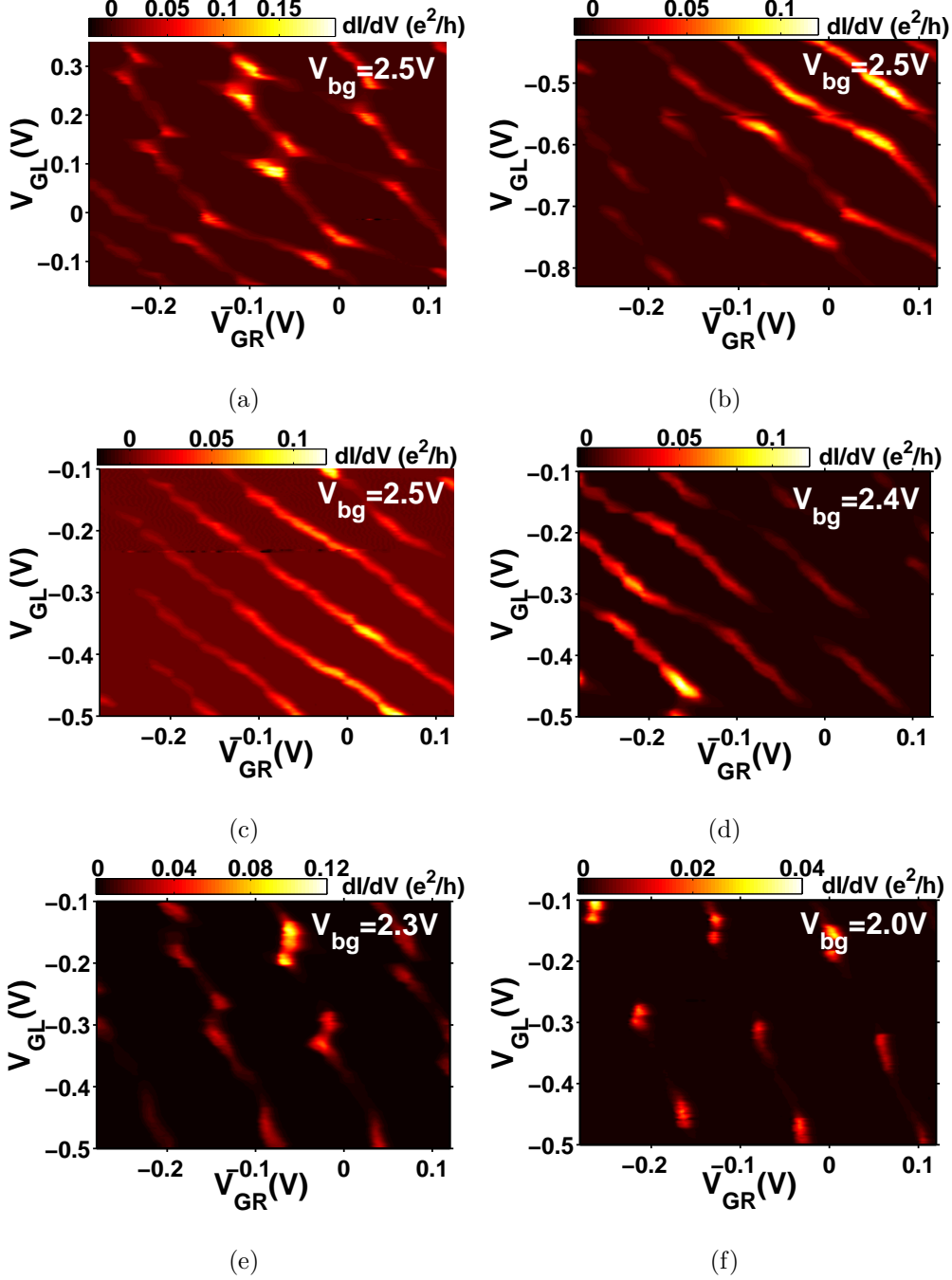


FIG. 3: (a)-(c) Colorscale plot of the differential conductance versus voltage applied on gate GL ( $V_{GL}$ ) and gate GR ( $V_{GR}$ ) at  $V_{bg} = 2.5\text{ V}$  for different  $V_{GL}$  regimes. (c)-(f) Colorscale plot of the differential conductance versus voltage applied on gate L ( $V_{GL}$ ) and gate R ( $V_{GR}$ ) for different back gate voltage  $V_{bg}$ . The trend of interdot tunnel coupling changing from weak to strong can be seen clearly.

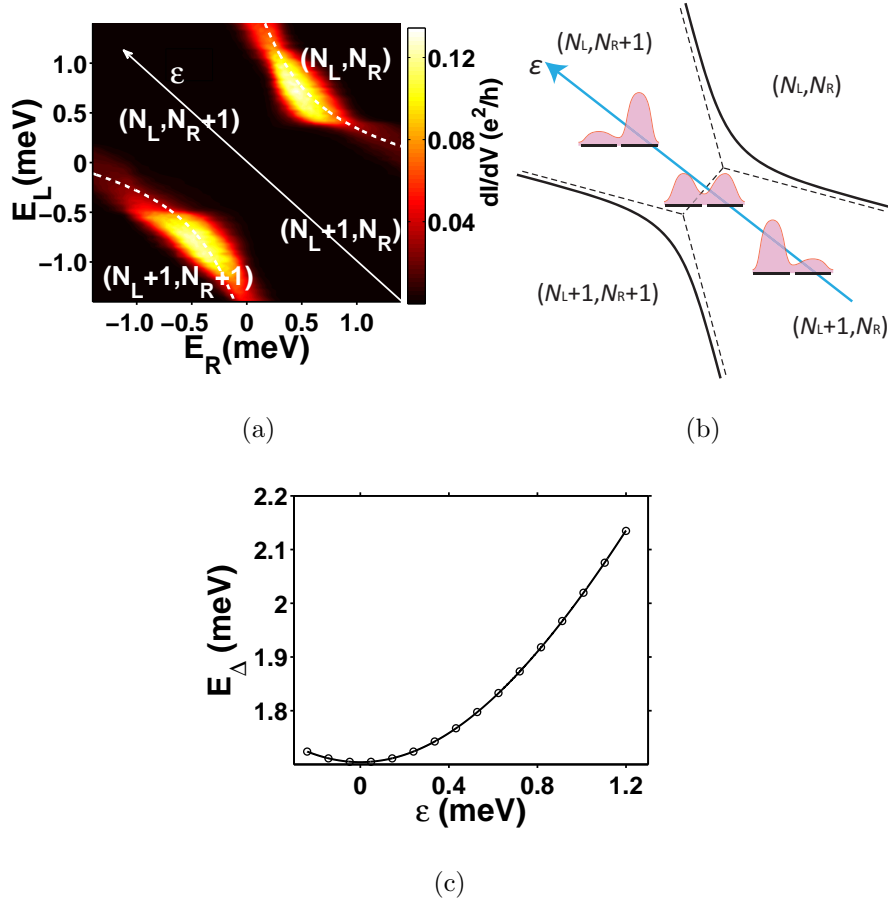


FIG. 4: (a) Colorscale plot of the differential conductance versus the energies of each dot  $E_L$  and  $E_R$  at  $V_{sd} = 20 \mu\text{V}$  near the selected two vertices with dashed lines as guides to the eye. (b) Schematic of a single anticrossing and the evolution from the state localized in each dot to a molecule state extending across both dots [17]. (c)  $E_\Delta$  dependence of the detuning  $\epsilon = E_L - E_R$ .  $E_\Delta$  (circles) is measured from the separation of the two high conductance wings in Fig. 4(a). The line illustrates a fit of the data to Eq. (1).

regime, we extract the quantitative properties based on a quantum model of graphene artificial molecule states [16, 17]. Here we only take into account the topmost occupied state in each dot and treat the other electrons as an inert core [13, 18]. In the case of neglected tunnel coupling, the nonzero conductance can only occur right at the vertices which are energy degenerate points as  $E(N_L + 1, N_R) = E(N_L, N_R + 1)$ . When an electron can tunnel coherently between the two dots, the eigenstates of the double dot system become the

superposed states of two well-separated dot states with the form

$$\begin{aligned} |\Psi_B\rangle &= -\sin\frac{\theta}{2}e^{-\frac{i\varphi}{2}}|N_L+1, N_R\rangle + \cos\frac{\theta}{2}e^{\frac{i\varphi}{2}}|N_L, N_R+1\rangle, \\ |\Psi_A\rangle &= \cos\frac{\theta}{2}e^{-\frac{i\varphi}{2}}|N_L+1, N_R\rangle + \sin\frac{\theta}{2}e^{\frac{i\varphi}{2}}|N_L, N_R+1\rangle, \end{aligned}$$

where  $\theta = \arctan(\frac{2t}{\epsilon})$ ,  $\epsilon = E_L - E_R$ ,  $E_L$  and  $E_R$  are the energies of state  $|N_L+1, N_R\rangle$  and  $|N_L, N_R+1\rangle$ , respectively. Thus  $|\Psi_B\rangle$  and  $|\Psi_A\rangle$  are the bonding and anti-bonding state in terms of the uncoupled dot, and the energy difference between these two states can be expressed by [16]

$$E_\Delta = U' + \sqrt{\epsilon^2 + (2t)^2}. \quad (1)$$

Here  $U' = \frac{2e^2C_m}{C_L C_R - C_m^2}$  is the contribution from electrostatic coupling between dots [19].

Provided that the graphene double-dot molecule eigenstate  $|\Psi\rangle$  participates in the transport process, sequential tunneling is also possible along the honeycomb edges [16]. In Fig. 4(a), a colorscale plot of the differential conductance is shown at  $V_{sd} = 20 \mu\text{V}$  in the vicinity of a vertex. As expected the visible conductance is observed at both the position of the vertex and the honeycomb edges extending from the vertex. Fig. 4(b) shows a fit of the energy difference  $E_\Delta$  from the measured amount of splitting of the positions of the differential conductance resonance peak in the  $\epsilon$ -direction. Here we use  $\epsilon = E_L - E_R = e\alpha_L V_{GL} - e\alpha_R V_{GR}$  to translate the gate voltage detuning  $V_{GL} - V_{GR}$  with the conversion factors  $\alpha_L$  and  $\alpha_R$  determined above. The fitting with Eq. (1) yields the values of tunnel coupling strength  $t \approx 727 \mu\text{eV}$  and  $U' \approx 209 \mu\text{eV}$ . Similar measurements have been performed in a carbon nanotube double dots with  $t \approx 358 \mu\text{eV}$  and  $U' \approx 16 \mu\text{eV}$  [16] and semiconductor double dots with  $t \approx 80 \mu\text{eV}$  and  $U' \approx 175 \mu\text{eV}$  [17]. The fact that the tunnel coupling  $t$  is dominant than capacitive coupling  $U'$  implies the interdot tunnel barrier in this etched graphene double dot is much more transparent than those gated carbon nanotube or semiconductor double dot.

Finally, we discuss the relevance of graphene double dot device for implementing a quantum gate and quantum entanglement of coupled electron spins. A  $\sqrt{\text{SWAP}}$  operation has already been demonstrated in a semiconductor double dot system using the fast control of exchange coupling  $J$  [20]. The operation time  $\tau$  is about 180 ps for  $J \approx 0.04 \text{ meV}$  corresponding to  $t \approx 0.16 \text{ meV}$ . In the present graphene device, we have obtained much larger  $t \approx 0.72 \text{ meV}$  and the estimated  $\tau \approx 50 \text{ ps}$  is much shorter than the predicted decoherence



time ( $\mu\text{S}$ ) [21]. The results indicate the ability to carry out two-electron spin operations in nanosecond timescales on a graphene device, four times faster than perviously shown for semiconductor double dot.

In conclusion, we have measured a graphene double quantum dot with multiple electrostatic gates and observed the transport pattern evolution in different gate configurations. This way offers us a method to identify the molecular states as a quantum-mechanical superposition of double dot and measure the contribution of the interdot tunneling to the splitting of the differential conductance vertex. The precisely extracted values of interdot tunnel coupling for this system is much larger than those in previously reported semiconductor device. These short operation times due to large tunneling strength together with the predicted very long coherence times suggest that the requirements for implementing quantum information processing in graphene nanodevice are within reach.

This work was supported by the National Basic Research Program of China (Grants No. 2009CB929600), the National Natural Science Foundation of China (Grants No. 10804104, No. 10874163, No. 10934006, No. 11074243).

- 
- [1] A. K. Geim, K. S. Novoselov, *Nature Materials* **6**, 183 (2007).
  - [2] A. K. Geim, *Science* **324**, 1530 (2009).
  - [3] T. Ihn, J. Guttinger, F. Molitor, S. Schnez, E. Schurtenberger, A. Jacobsen, S. Hellmüller, T. Frey, S. Droscher, C. Stampfer, and K. Ensslin, *Materials Today* **13**, 44 (2010).
  - [4] R. Hanson, L. P. Kouwenhoven, J. R. Petta, S. Tarucha, and L. M. K. Vandersypen, *Rev. Mod. Phys.* **79**, 1217 (2007).
  - [5] R. Hanson, and D. Awschalom, *Nature* **453**, 1043 (2008).
  - [6] J. Fischer, and D. Loss, *Science* **324**, 1277 (2009).
  - [7] B. Trauzettel, D. V. Bulaev, D. Loss, and G. Burkard, *Nature Physics* **3**, 192 (2007).
  - [8] G. P. Guo, Z. R. Lin, T. Tu et al. *New Journal of Physics* **11**, 123005 (2009).
  - [9] L. Ponomarenko, F. Schedin, M. Katsnelson, R. Yang, E. Hill, K. Novoselov, and A. Geim, *Science* **320**, 356 (2008).
  - [10] C. Stampfer, E. Schurtenberger, F. Molitor, J. Guettinger, T. Ihn, and K. Ensslin, *Nano Lett.* **8**, 2378 (2008).

- [11] F. Molitor, H. Knowles, S. Droscher, U. Gasser, T. Choi, P. Roulleau, J. Guttinger, A. Jacobsen, C. Stampfer, K. Ensslin, and T. Ihn, *Europhys. Lett.* **89**, 67005 (2010).
- [12] X. L. Liu, D. Hug, and L. M. K. Vandersypen, *Nano Lett.* **10**, 1623 (2010).
- [13] W. G. van der Wiel, S. de Franceschi, J. M. Elzermann, T. Fujisawa, S. Tarucha and L. P. Kouwenhoven, *Rev. Mod. Phys.* **75**, 1 (2003).
- [14] N. Mason, M. J. Biercuk, and C. M. Marcus, *Science* **303**, 655 (2004).
- [15] L. P. Kouwenhoven et al., in *Mesoscopic Electron Transport*, L. P. Kouwenhoven, G. Schön, L. L. Sohn, Eds. (Kluwer, Dordrecht, Netherlands, 1997).
- [16] M. R. Graber, W. A. Coish, C. Hoffmann, M. Weiss, J. Furer, S. Oberholzer, D. Loss, and C. Schönenberger, *Phys. Rev. B* **74**, 075427 (2007).
- [17] T. Hatano, M. Stopa, and S. Tarucha, *Science* **309**, 268 (2005).
- [18] V. N. Golovach, and D. Loss, *Phys. Rev. B* **69**, 245327 (2004).
- [19] R. Ziegler, C. Bruder, and H. Schoeller, *Phys. Rev. B* **62**, 1961 (2000).
- [20] J. R. Petta, A. C. Johnson, J. M. Taylor, E. A. Laird, A. Yacoby, M. D. Lukin, C. M. Marcus, M. P. Hanson and A. C. Gossard, *Science* **309**, 2180 (2005).
- [21] J. Fischer, B. Trauzettel, and D. Loss, *Phys. Rev. B* **80**, 155401 (2009).